

Diurnal Evolution and Structure of Long-Lived Mesoscale Convective Vortices along the Mei-Yu Front over the East China Plains

YUANCHUN ZHANG

Key Laboratory of Cloud-Precipitation Physics and Severe Storms (LACS), Institute of Atmospheric Physics, Chinese Academy of Sciences, Beijing, China, and Department of Meteorology and Atmospheric Science, and Center for Advanced Data Assimilation and Predictability Techniques, The Pennsylvania State University, University Park, Pennsylvania

FUQING ZHANG

Department of Meteorology and Atmospheric Science, and Center for Advanced Data Assimilation and Predictability Techniques, The Pennsylvania State University, University Park, Pennsylvania

CHRISTOPHER A. DAVIS

National Center for Atmospheric Research, Boulder, Colorado

JIANHUA SUN

Key Laboratory of Cloud-Precipitation Physics and Severe Storms (LACS), Institute of Atmospheric Physics, Chinese Academy of Sciences, Beijing, China

(Manuscript received 5 July 2017, in final form 8 January 2018)

ABSTRACT

The structure and diurnal evolution of long-lived, eastward-propagating mesoscale convective vortices (MCVs) along typical summertime mei-yu fronts over the east China plains are investigated through composite analysis of a 30-day semi-idealized simulation. The simulation uses lateral boundary conditions that vary only diurnally in time using analyses of recurring MCV events during 1–10 July 2007. Hence, the behavior of convection and vorticity follows a closely repeating diurnal cycle for each day during the simulation. Assisted by the eastward extension of enhanced vorticity anomalies from the Sichuan basin, the incipient MCV forms in the morning hours over the immediate lee (east) of the central China mountain ranges (stage 1). From local afternoon to early evening, as the MCV moves over the plains, convection weakens in the daytime downward branch of the mountain–plains solenoid. This allows the upper-level and lower-level portions of the vortex to partially decouple, and for convection to shift to the east-southeast side of the surface vortex (stage 2). Immediately after sunset, convection reinvigorates above the low-level MCV center as a result of moistening and destabilization from a combination of radiative forcing and an intensified low-level jet. This intensifies the MCV to maturity (stage 3). The mature MCV eventually evolves into an occluding subsynoptic cyclone with strong convection across all sectors of the low-level vorticity center during the subsequent day's morning hours along the east China coastal plains before it moves offshore (stage 4).

1. Introduction

Mesoscale convective vortices (MCVs) are cyclonic vorticity centers that form in the mid- to lower atmosphere forced by mesoscale convective systems (MCSs; Brown 1979; Bartels and Maddox 1991; Davis and Weisman 1994). The MCVs are meso- β - to meso- α -scale weather phenomena that have typical time scales

ranging from hours to days, and horizontal scales of around 100–300 km in diameter extending several kilometers vertically (Bosart and Sanders 1981; Fritsch et al. 1994; Jorgensen and Smull 1993; Yu et al. 1999; Trier et al. 2000; Davis and Trier 2007). Raymond and Jiang (1990) proposed that an environment consisting of weak midlevel shear but stronger low-level shear could promote a mesoscale rotational circulation during an MCS event. Davis and Weisman (1994) demonstrated that the development of low- to midtropospheric

Corresponding author: Fuqing Zhang, fzhang@psu.edu

cyclonic potential vorticity (PV) may characterize the formation of an MCV. In more idealized and/or theoretical approaches based on PV thinking, studies showed that latent heat release from an MCS is usually maximized in the midtroposphere that redistributes the PV so that a positive PV anomaly forms in the mid- to lower troposphere beneath a negative PV anomaly at upper levels (Thorpe 1985; Haynes and McIntyre 1987; Raymond and Jiang 1990; Chen and Frank 1993). The latent heat and the associated convective updraft also contribute to enhancement and maintenance of the vortex through stretching (Fritsch et al. 1994; Rogers and Fritsch 2001; Davis and Trier 2002) and/or the convergence of larger-scale or planetary vorticity (Bartels and Maddox 1991; Skamarock et al. 1994). However, some studies showed that tilting of preexisting horizontal vorticities could also contribute to the MCV development (e.g., Brandes 1990; Zhang 1992; Kirk 2007).

The mei-yu front is a warm-season quasi-stationary, east–west-oriented frontal zone that forms over central and east China characterized by a weak temperature gradient but with a strong contrast in moisture across the frontal boundary. It is one of the most significant weather systems in the East Asia monsoon region that is often responsible for severe flooding along the Yangtze–Huai River valley (YHRV), and is characterized by strong low-tropospheric cyclonic wind shear (Chen 1983). Numerous mesoscale disturbances including both MCSs and/or MCVs have been observed to form, develop, and propagate eastward along this quasi-stationary frontal boundary, often associated with strong precipitation (Ding 1993; Ninomiya 2000; Chen and Zheng 2004; Zhao et al. 2004; Sun et al. 2010; Xu et al. 2017).

Most of the larger cyclonic circulations (including MCVs) along the mei-yu front are observed to develop in the lee (east) of the second-step terrain in east China ($\sim 115^{\circ}\text{E}$; Zhang et al. 2004; Sun and Zhang 2012, hereafter SZ12). The second-step high terrain includes the Taihang Mountains, the Loess Plateau over north China, the Qinling Mountains over central China, and the Yungui Plateau over southwest China (Fig. 1). SZ12 explored the impact of mountain–plains solenoids (MPSs) between the second-step high-mountain ranges and the adjacent eastern plains on the diurnal variations of precipitation and MCVs along the mei-yu front over the YHRV region during 1–10 July 2007. This period featured several heavy precipitation episodes with the maximum 10-day accumulated precipitation exceeding 400 mm. SZ12 proposed that the MPSs induced by differential heating between the high mountain ranges in central China and the low-lying plains in east China

could be responsible for the repeated development of the MCVs and convection along the mei-yu front.

Building on the findings of SZ12, the primary objective of the present study is to further explore the diurnal evolution and structure of MCVs east of the second-step terrain along the mei-yu front over central and east China. The experimental design is described in section 2. An overview of the simulations and their comparison with observations are presented in section 3. The detailed formation, diurnal evolution, and decay of the MCV along the mei-yu front are discussed in section 4. Concluding remarks are presented in section 5.

2. Experimental design

This study uses the Advanced Research version of the Weather Research and Forecasting (WRF) Model (version 3.5.1; Skamarock et al. 2005). The simulation domain is as in SZ12 (see Fig. 1), which covers the eastern part of China with 250×230 horizontal grids with 9-km grid spacing covering an area of $2250 \text{ km} \times 2070 \text{ km}$ that includes the eastern slope of the Tibetan Plateau, the Sichuan basin, the second-step high mountains, the eastern low-lying plains, and the hilly areas in southeast China as the third-step terrain. Different from SZ12, the current study increases the model vertical levels from 27 to 31 (with the model top at 50 hPa) but keeps the same physics configurations that use the Yonsei University (YSU) boundary layer scheme (Noh et al. 2001), the Noah land surface model (Chen and Dudhia 2001), long- and shortwave radiation parameterization (Dudhia 1989), a WRF single-moment 5-class microphysics scheme (WSM5; Hong et al. 2004; Hong and Lim 2006), and a new Grell cumulus parameterization (Grell and Dévényi 2002). Other model configurations, including the use of the WSM6 microphysics (Hong and Lim 2006) and the use of a large 3-km convection-permitting nest were performed as well. The results shown herein for the control simulation are consistent with the results of those other simulations.

To achieve more stable and representative solutions, all three experiments in this study (Table 1) were integrated for 30 days. They were initiated with the average conditions at 0000 UTC of the 10-day (1–10 July 2007) period, with the 10-day-averaged 0000, 0600, 1200, and 1800 UTC diurnal cycle lateral boundary conditions derived from the National Oceanic and Atmospheric Administration (NOAA) Global Forecast System (GFS) $1^{\circ} \times 1^{\circ}$ operational analyses with a 6-h interval.

As in SZ12, the terrain distribution of TOPO_REAL corresponds to the actual terrain while the terrains of TOPO_CNTL east of 112°E and south of 33.2°N over southern China are set uniformly to a height of 10 m to

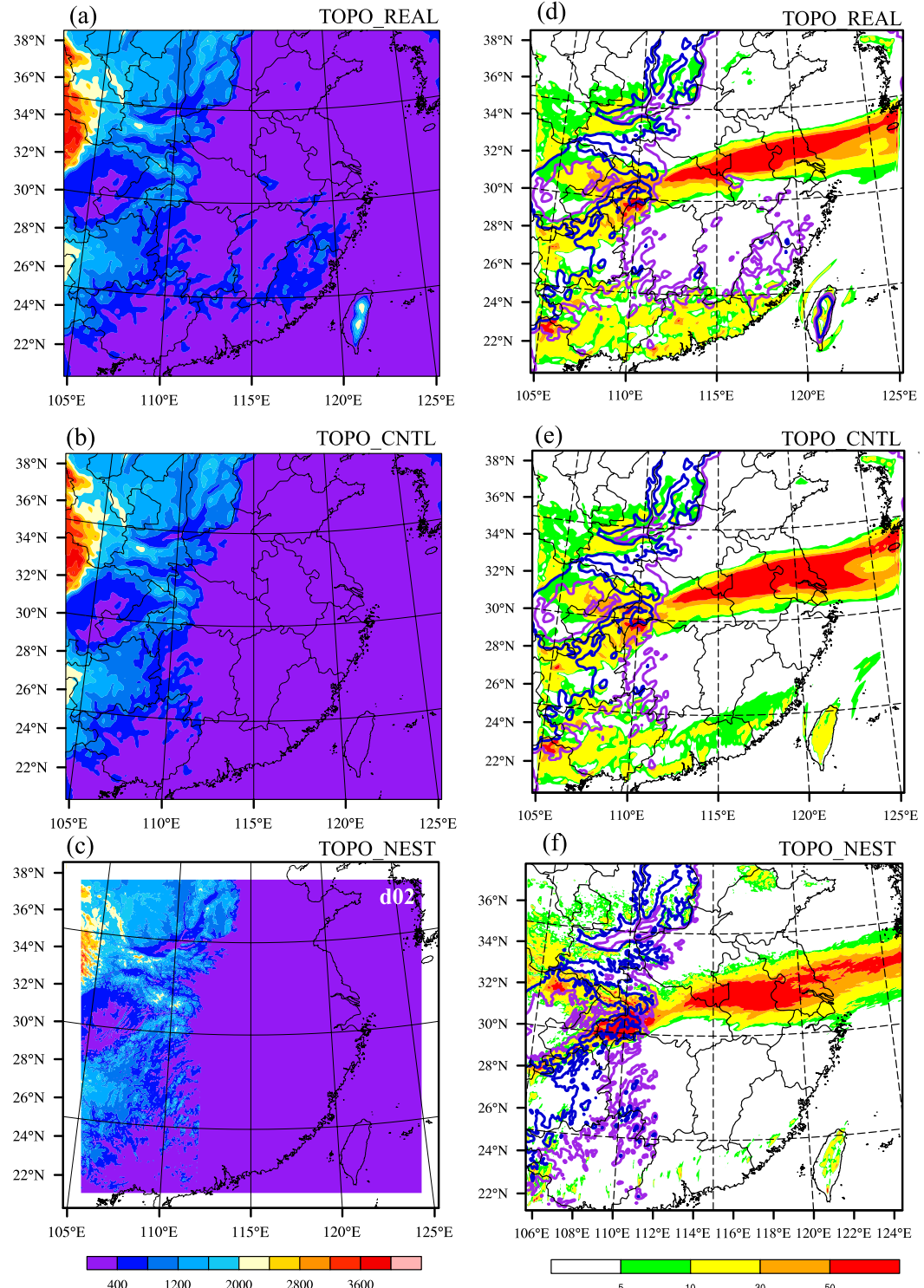


FIG. 1. (left) Distributions of the terrain heights (m) and the model domain for each of three simulations: (a) TOPO_REAL, (b) TOPO_CNTL, and (c) domain 2 of TOPO_NEST. (right) The average daily rainfall (mm) for the last 25 days for simulations (d) TOPO_REAL, (e) TOPO_CNTL, and (f) domain 2 of TOPO_NEST. Solid lines are the terrain heights of 500 (purple lines) and 1000 m (blue lines).

TABLE 1. Experimental details.

| Expt | Objective | Terrain | Initial and boundary conditions | Horizontal resolution | Integration time |
|-----------|--|---|--|--------------------------------|------------------|
| TOPO_REAL | Real terrain distribution | Real terrain distribution | As in SZ12; initial condition: mean of 0000 UTC each day during 1–10 Jul 2007; Boundary conditions: mean of 0000, 0600, 1200, and 1800 UTC each day during 1–10 Jul 2007 | 9 km | 1 month |
| TOPO_CNTL | Sensitivity to topography over southeast China | Removing the topography to the east of 112°E and to the south of 33.2°N over southern China | As in TOPO_REAL | 9 km | 1 month |
| TOPO_NEST | Sensitivity to horizontal resolution | As in TOPO_CNTL | As in TOPO_REAL | Domain 1: 9 km; domain 2: 3 km | 1 month |

examine the impacts of smaller mountain ranges over southern China and to exemplify the effect of the second-step terrain on evolution of the MCVs. Experiment TOPO_CNTL is the same as CNTL in SZ12. Based on the terrain distribution of TOPO_CNTL, and to further investigate the sensitivity of the model horizontal resolution, an additional experiment with a 3-km convection-permitting nested domain embedded in the TOPO_CNTL domain (Fig. 1c) was also performed. The 3-km nested domain is nearly as big as the entire 9-km domain except for allowing some transitional boundaries on each side.

3. Simulation comparison

a. Background and precipitation comparison

The nearly periodic eastward-moving precipitating system appears after the fifth integration day (5 July) (Figs. 2a,c,e). Figures 1d–f show the final 25-day-averaged daily precipitation of the three experiments. The main average daily rain belt of TOPO_REAL runs from the second-step terrain to the eastern coastline. The maximum daily rainfall along the southwest–northeast-orientated rain belt exceeds 50 mm. It has been shown that a diurnally forced boundary simulation leads to more concentrated and locally heavier precipitation compared to a simulation with fully varying boundary forcing (Trier et al. 2006; Bao et al. 2011; SZ12; Zhang et al. 2014). After removing the topography east of 112°E and south of 33.2°N (Fig. 1c), the location and intensity of the main rain belt of TOPO_CNTL are almost the same as those for TOPO_REAL but with smoother and broader rainfall in excess of 50 mm day^{-1} over the eastern low-lying regions. Then, the precipitation related to smaller-scale convection is reproduced in the 3-km nested domain (Fig. 1c). The main rain belt is overall very consistent with the two previous experiments except for

somewhat stronger precipitation over the eastern edge of the second-step terrain and weaker rainfall in the eastern ocean.

For the former two experiments, the 25-day-averaged geopotential heights in the middle (500 hPa) and lower (850 hPa) troposphere and the wind field at 850 hPa are shown in Fig. 3. In all the simulation results, the background circulations in the middle and lower troposphere remain nearly unchanged: a southwesterly flow covering midlatitudes, the western Pacific subtropical high controlling conditions in southeast China at 500 hPa, and the 5880-m isohypse reaching as far west as 110°E; the southwest vortex anchored over the Sichuan basin; southwesterly and northeasterly winds converging along the mei-yu front over the YHRV east of the Sichuan basin vortex; and the low-level jet (LLJ) stronger than 12 m s^{-1} extending north to 30°N. After removing the hilly areas in southeast China (TOPO_CNTL), the average geopotential height at 500 hPa east of the second-step terrain (112°E) is much smoother than that of TOPO_REAL.

For each of the three experiments, Fig. 2 shows Hovmöller diagrams of hourly rainfall averaged over the rain belt shown in Fig. 1. All the simulations successfully reproduced the local afternoon convection over the eastern part of the second-step terrain (107.5°–110°E). The precipitation moves eastward continually, reaching the eastern coastline the next morning, with the maximum appearing over the YHRV (115°–120°E) in the late evening to early the next morning. Another common feature is that the periodic eastward propagation of the precipitation originating from the second-step terrain reappears every day after 120 h of integration (i.e., every day after 5 July). Besides the eastward propagation, there is a second rainfall peak in the late-afternoon to early evening over the region of 117°–122°E that is consistent with previous studies of double-peak precipitation along the mei-yu front (Geng and Yamada 2007). However, compared with TOPO_REAL, the

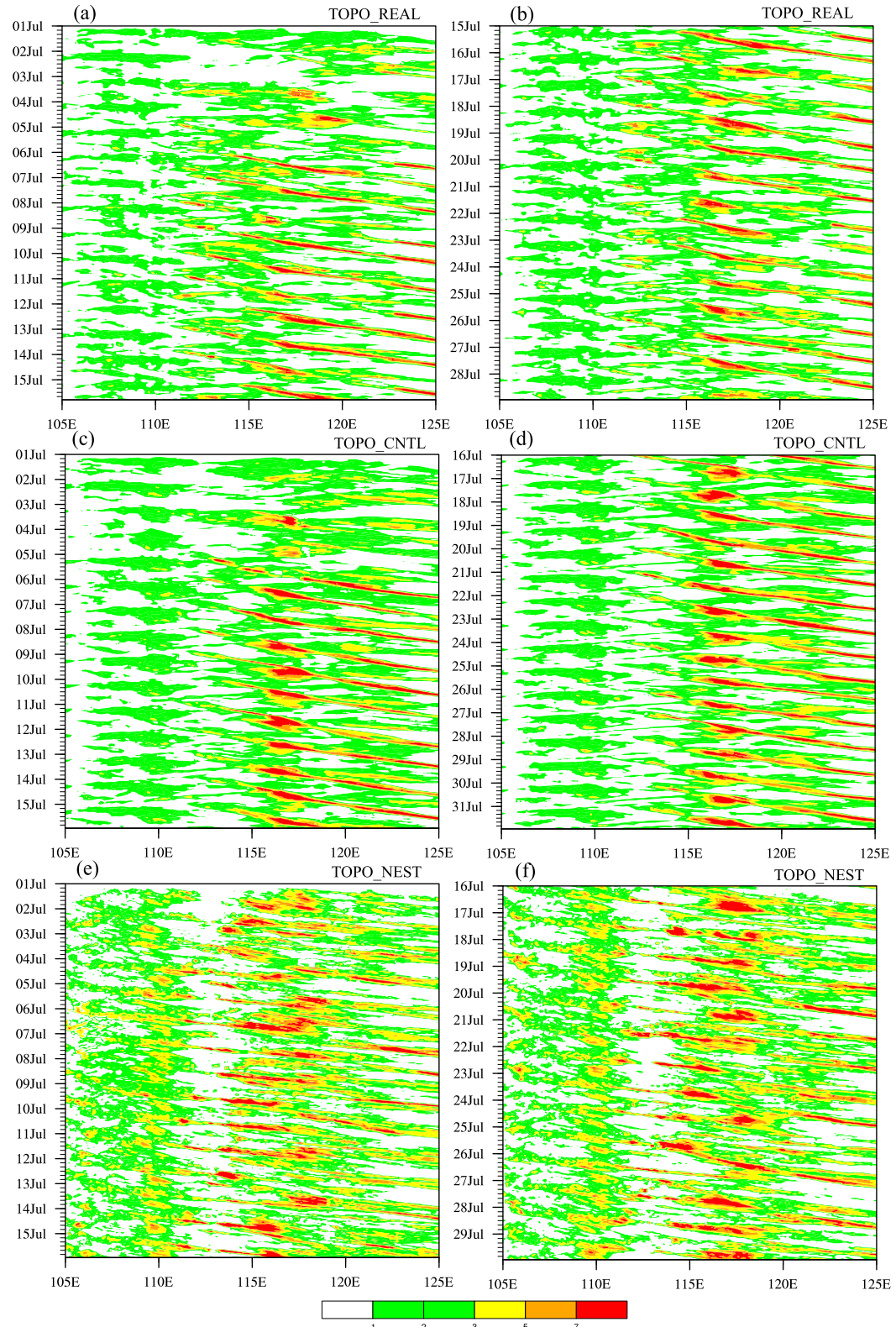


FIG. 2. Time-longitude diagrams of hourly rainfall (mm) over the primary mei-yu front rain belt averaged between 30° – 34° N as shown in (a),(b) TOPO_REAL; (c),(d) TOPO_CNTL; and (e),(f) TOPO_NEST.

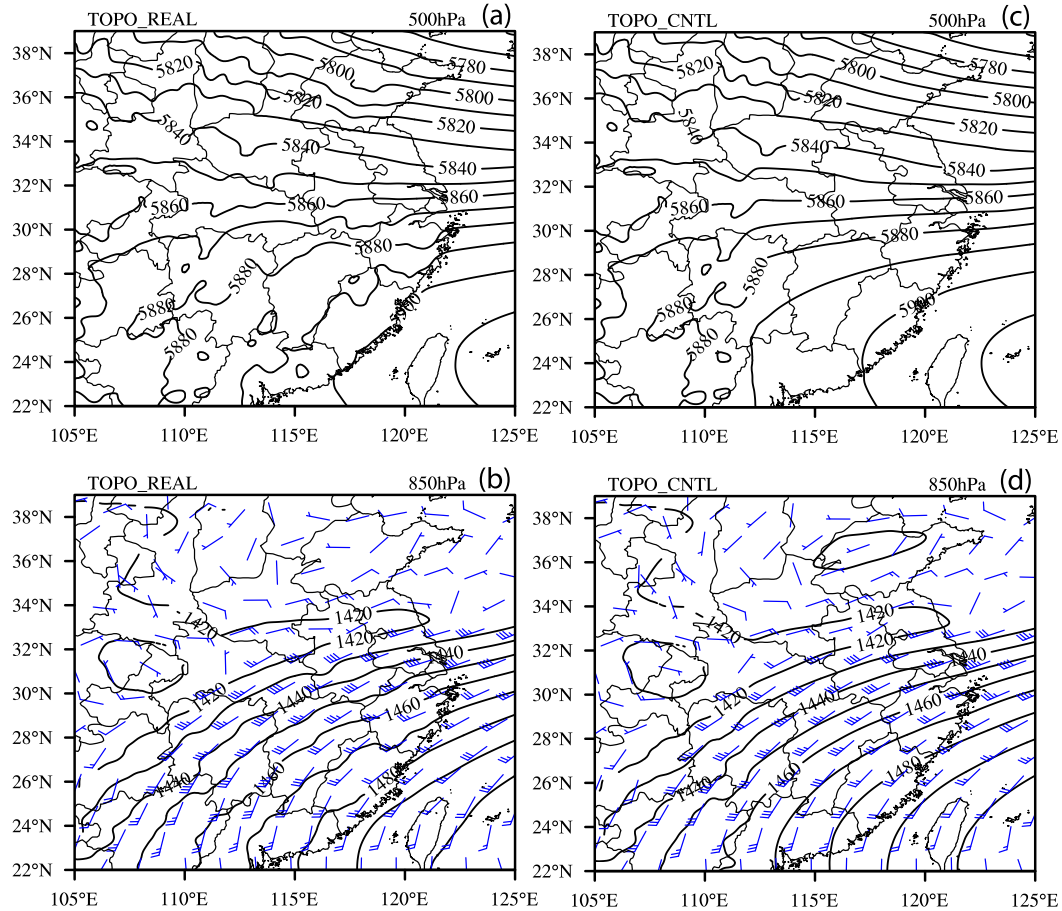


FIG. 3. (top) The 500-hPa time-averaged geopotential heights (m) for (a) TOPO_REAL and (c) TOPO_CNTL. (bottom) The corresponding 850-hPa wind field and geopotential heights (m) for (b) TOPO_REAL and (d) TOPO_CNTL.

continuity and repeatability of the eastward propagation rainfall in TOPO_CNTL is more robust, especially in the final 15 days. As for the convection-permitting experiment TOPO_NEST, precipitation (Figs. 1f and 3e,f) and the smaller-scale vortex along the mei-yu front (Fig. 6) are less intense and less periodic compared to TOPO_CNTL. However, the overall MCV evolution and diurnal variation are consistent with those in TOPO_CNTL. Considering the reduced complexity of the terrain, the more consistent eastward propagation of precipitation, and the presence of quasi-stationary mei-yu convergence, the following analysis is based on the time-averaged field of TOPO_CNTL.

b. Diurnal cycle of precipitation and the MCV

Figure 4 shows the final 25-day-averaged diurnal cycles of the simulated maximum column reflectivity, wind field, and equivalent potential temperature θ_e at 925 hPa at 3-h intervals. There is a horizontal gradient of θ_e located around 32° – 34° N and east of 112° E. Abundant

warm and moist air to the south and cool and dry air to the north are identified with the persistent and intense mei-yu front. The southwesterly flow and easterlies converge south of the strong gradient of θ_e . Moreover, the θ_e gradient and convergence line become more intense during the night (Figs. 4a–d).

Mesoscale convection with high θ_e forms over the lee side of the second-step terrain and evolves gradually to the eastern coastline along the mei-yu front. Convection originating over the eastern second-step terrain (30° – 32° N, $\sim 110^{\circ}$ E) is enhanced from the early evening [2000 Beijing standard time (BST) (1200 UTC); Fig. 4a]. This is because the eastward extension of the southwestern vortex (SWV) and the corresponding convection over the eastern part of the second-step terrain during the evening [2000–2300 BST (1200–1500 UTC); pointed out by red arrows with dashed line in Figs. 4a and 4b] overlap with the upward branch of nocturnal MPS circulation between the second-step terrain and its eastern low-lying intensified convection on the lee side

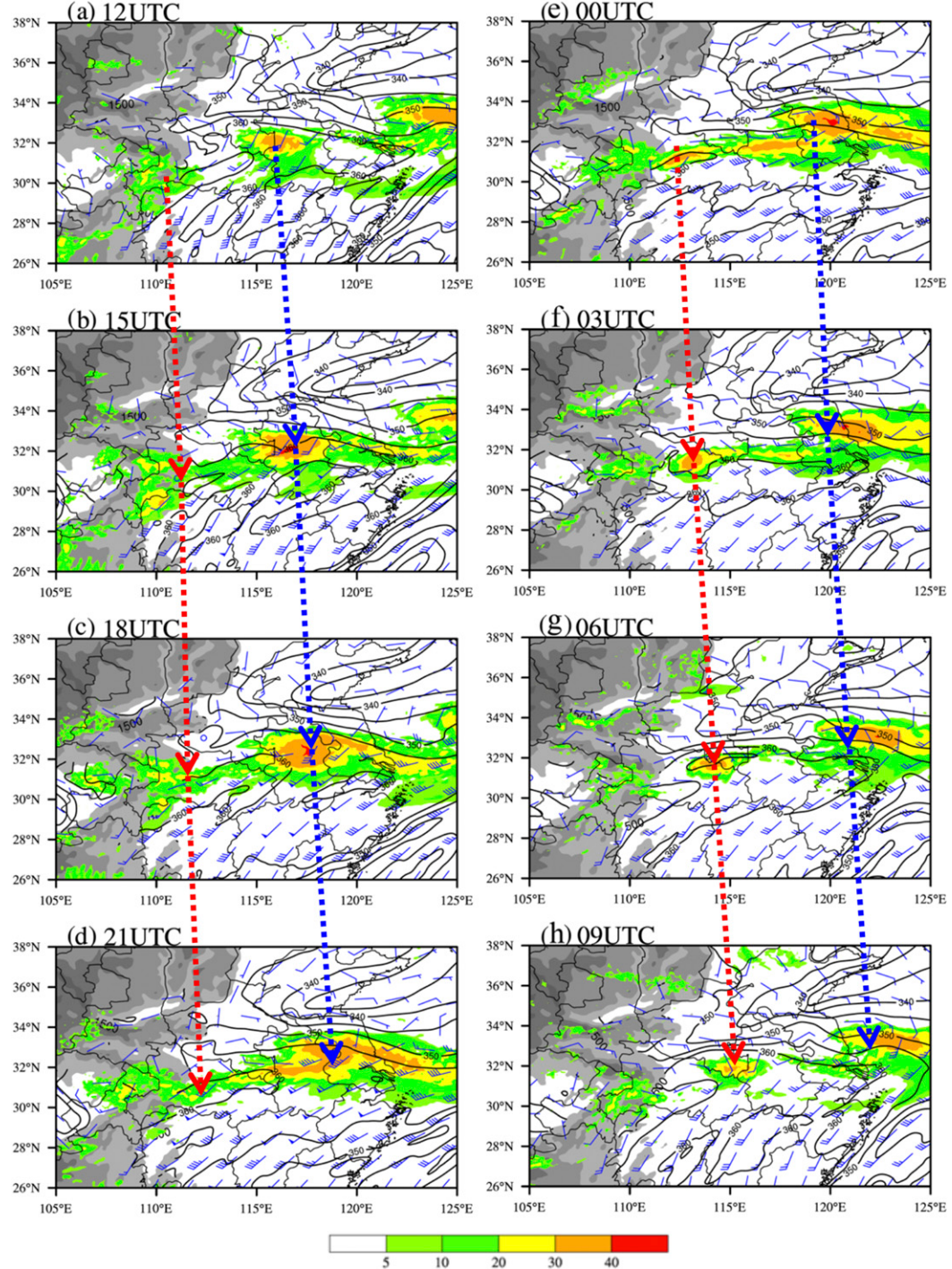


FIG. 4. Diurnal variations of the 925-hPa horizontal wind (blue wind barbs), equivalent potential temperature (black line; K), and maximum reflectivity (colored; dBZ) every 3 h from the control experiment (TOPO_CNTL).

(31°N , 112°E). This intensified convection enhances the low-level wind perturbation on the western edge of the mei-yu front along the eastern edge of the second-step terrain [0200–0500 BST (1800–2001 UTC); pointed out by red arrows with dashed line in Figs. 4c and 4d]. The

wind perturbation, which is characterized by horizontal wind shear, evolves into a mesoscale vortex in the early morning [after 0500 BST (2100 UTC); Fig. 4d]. A closed mesoscale convective vortex and its corresponding convection form in the morning [0800 BST

(0000 UTC); Fig. 4e] with high θ_e (note the 360-K contour).

After 1500 BST (0700 UTC, not shown), the development of the coupled MCV and convection is suppressed during the day as the system migrates eastward to the low-lying areas. The northward extension of high θ_e (360-K contour) indicates an enhanced θ_e gradient and mei-yu frontal convergence [1700 BST (0900 UTC); Fig. 4h]. In the early evening [2000 BST (1200 UTC); pointed out by blue arrows with dashed line in Fig. 4a], the convection undergoes a second enhancement. Meanwhile, the strengthened nocturnal LLJ and convection lead to MCV intensification in the late evening near 117°E [2300 BST (1500 UTC); pointed out by blue arrows with dashed line in Fig. 4c]. The convection coupled with the new MCV then propagates eastward, south of the strong θ_e gradient along the mei-yu front. It is possible that the nocturnal LLJ, with its abundant water vapor transport, favors rainfall along the convergence line in warmer areas [0200–0500 BST (1800–2100 UTC); pointed out by blue arrows with dashed line in Figs. 4c and 4d]. The occluded MCV and convection then continue to move eastward to the coastline, with a convection line remaining over the YHRV [0800–1400 BST (0000–0600 UTC); pointed out by blue arrows with dashed line in Figs. 4e–g].

In summary, the MCV is triggered at the lee side of the second-step terrain in the early morning at the western edge of the mei-yu front. The MCV coupled with enhanced convection then propagates eastward to the low-lying areas, but the couplet weakens during the day. However, the MCV and its convection undergo secondary development at night. After the vortex and convection form a new couplet, an occluded structure appears over the YHRV. The couplet then continues to propagate eastward to the coast and decays over the ocean.

4. Evolution and structure of the MCV and its convection

a. Life cycle diagnosis

According to the diurnal cycles of the MCV, convection, and mei-yu front at 925 hPa as described in section 3b, it takes a total of about 36 h for the MCV to undergo its life cycle, namely, formation on the lee side of the second-step terrain, development while propagating eastward along the mei-yu front, maturation over the YHRV, and decay over the ocean. Herein we adopt a vortex-following approach and focus on the 24-h period during which the bulk of the vortex evolution occurs.

In Fig. 5 we show plan views of vorticity, wind, and model-derived radar reflectivity for this 24-h period

for TOPO_CNTL, while Fig. 6 is for TOPO_NEST. Hovmöller diagrams, also centered on the maximum vorticity at 850 hPa, reveal the intensity and radial extent of the vortex (Fig. 7a) and the phasing of the rainfall with the vorticity along the path of system movement (Fig. 7b). To summarize these figures, it is convenient to define four stages of evolution. Stage 1, the initial formation of the MCV (V1) and its coupled convection (C1) (couplet is denoted “C1/V1”), is nearly complete by early afternoon on day 1 (0500 UTC). This is followed by a decoupling stage from roughly 0600 to 1200 UTC (stage 2) during which the vortex tilts and weakens and convection becomes displaced to the east of the low-level MCV center. Stage 2 is denoted as the decoupling stage, in reference to the displacement of the convection from the lower-tropospheric cyclonic vorticity. During the subsequent evening after 1200 UTC, convection re-intensifies and moves closer to the MCV center, and the MCV intensifies as well (stage 3). Stage 3 is denoted as the recoupling stage. While clearly related to the earlier convection and vorticity, the resulting intensified couplet is denoted “C2/V2.” In particular, C2/V2 constitutes a much larger system than C1/V1 (Fig. 7). In stage 4, roughly beginning at 1800 UTC, the vortex reaches its maximum intensity, and becomes strong enough to distort the mei-yu front into a locally occluded frontal structure. The evolution of vorticity and convection in the convection-permitting experiment TOPO_NEST (Fig. 6) is similar to that in TOPO_CNTL, though the timing of vortex intensification shifts slightly to later in the day. This may be because convection is known to occur later in convection-permitting simulations; convection is only marginally resolved while no parameterization is used.

To explore the dynamics that govern the life cycle of the MCV, a quasi-Lagrangian vorticity budget [Eq. (1)] is calculated. We first consider the traditional form of the vorticity equation:

$$\underbrace{\frac{\delta \zeta_z}{\delta t}}_{\text{LHS}} = \underbrace{-\mathbf{V}_h \cdot \nabla_h \zeta_z}_{\text{HADV}} - \underbrace{w \frac{\partial \zeta_z}{\partial z}}_{\text{VADV}} + \underbrace{\mathbf{k} \cdot \left(\frac{\partial \mathbf{V}_h}{\partial z} \times \nabla_h w \right)}_{\text{TILT}} - \underbrace{(\zeta_z + f) \nabla_h \cdot \mathbf{V}_h}_{\text{STRE}} + \text{RES}, \quad (1)$$

where ζ_z is the vertical vorticity and δ is the quasi-Lagrangian vorticity tendency. The MCV moving speed is subtracted from the horizontal wind speed. The term $\mathbf{V}_h = u\mathbf{i} + v\mathbf{j}$ is the horizontal velocity vector, where \mathbf{i} , \mathbf{j} , and \mathbf{k} stand for the unit vector components pointing to the east, north, and zenith, respectively; w is the vertical velocity; $\nabla_h = (\partial/\partial x)\mathbf{i} + (\partial/\partial y)\mathbf{j}$ is the horizontal gradient operator; and f is the Coriolis parameter. The term

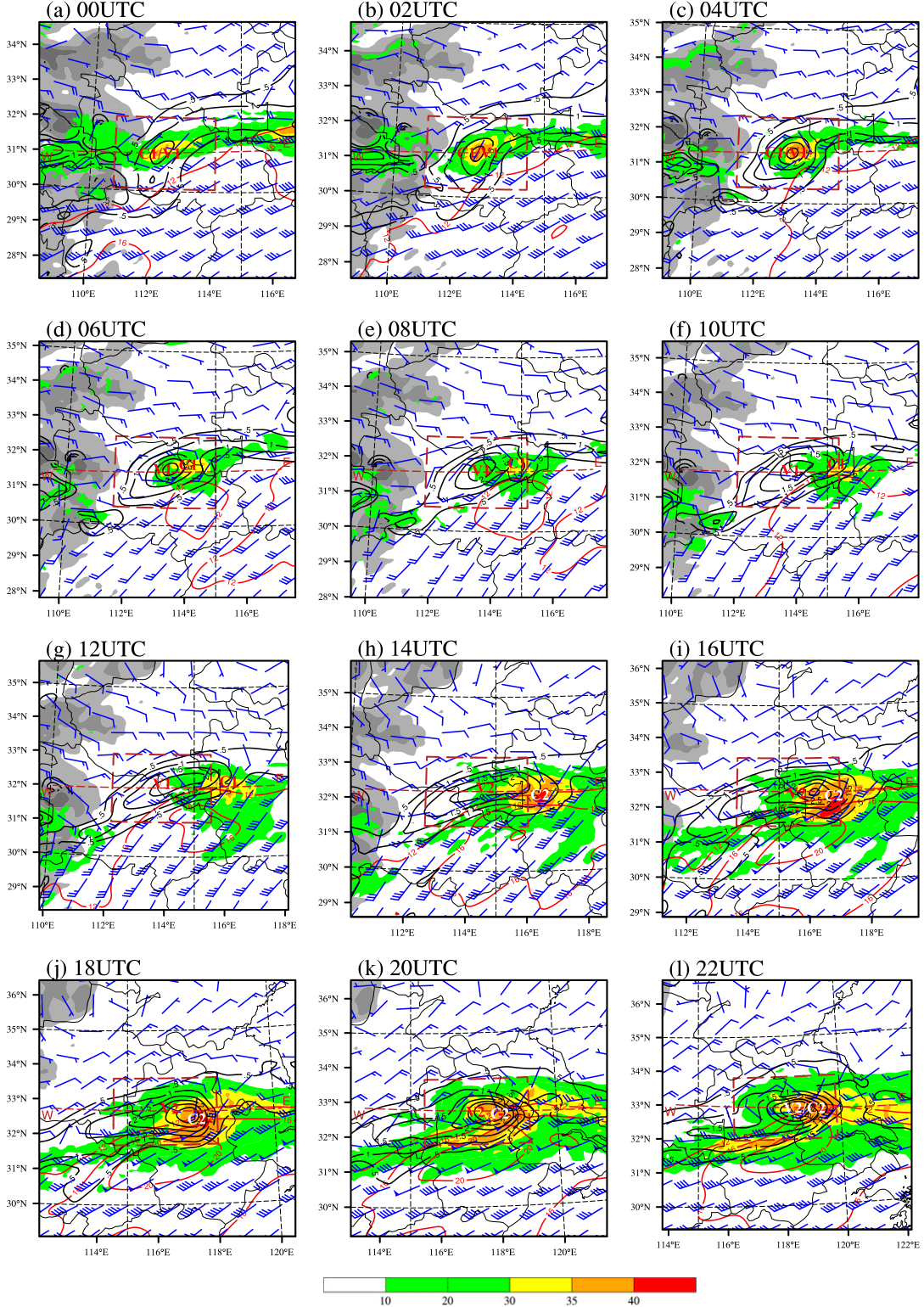


FIG. 5. The MCV evolution at 850 hPa over the focus domain ($\sim 800 \text{ km} \times 800 \text{ km}$) centered at and shifted with the 850-hPa vorticity maximum. The maximum reflectivity (colored; dBZ), vorticity (black lines; 10^{-4} s^{-1}), wind vector (blue wind barbs), and wind speed (red lines only for values $> 12 \text{ m s}^{-1}$). The brown dashed box is the area used for the vorticity budget, and the brown dashed line marked by W-E is for the cross sections.

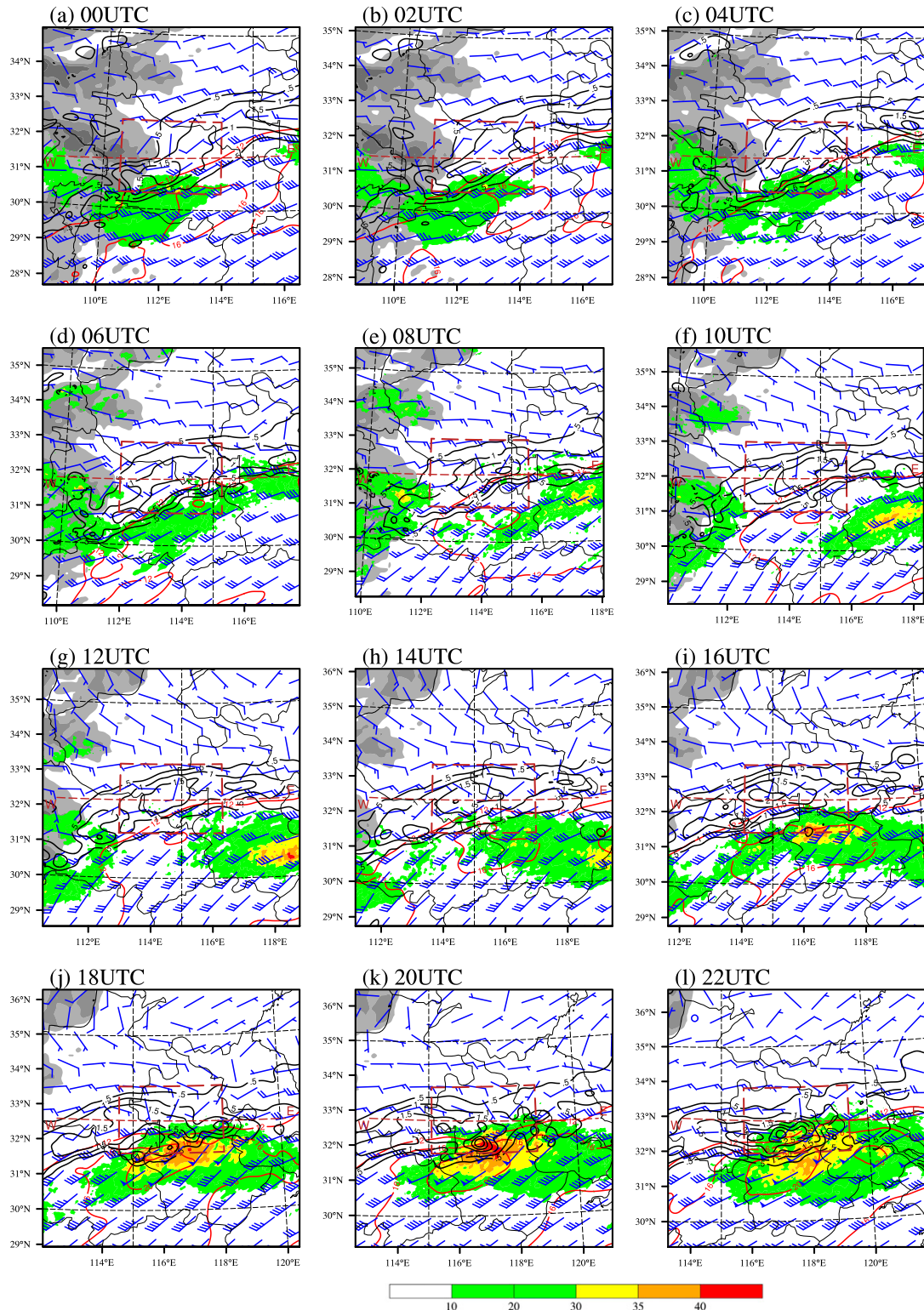


FIG. 6. As in Fig. 5, but for the domain 2 of TOPO_NEST.

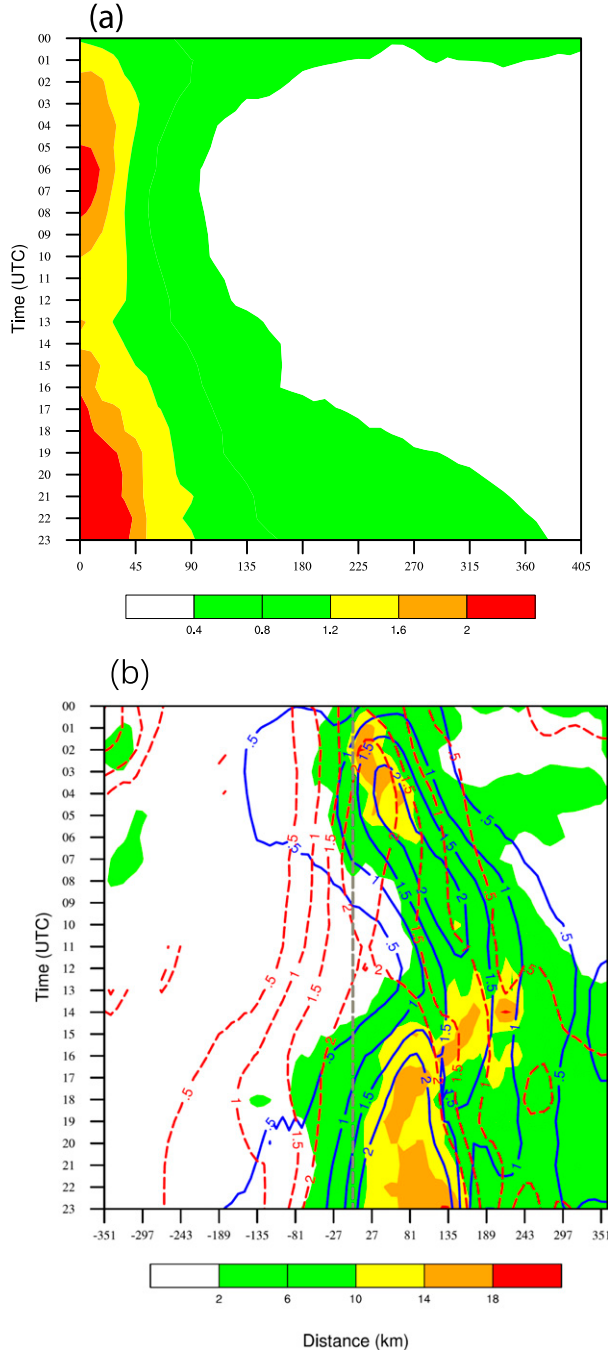


FIG. 7. (a) Time–radius diagram of potential vorticity (PV units; $1 \text{ PVU} = 10^{-6} \text{ K kg}^{-1} \text{ m}^2 \text{ s}^{-1}$) of MCV at 850 hPa. (b) Time–distance diagram of hourly rainfall (colored; mm), and vorticity (10^{-4} s^{-1}) at 500 (blue lines) and 850 hPa (red dashed lines). The gray dashed line is the location of the averaging box.

HADV in Eq. (1) represents the horizontal advection of vorticity, VADV denotes the vertical advection of vorticity, TILT is the tilting term, STRE is the stretching effect associated with divergence or convergence, and RES is the

residual term. The term on the left-hand side (LHS) of Eq. (1) is the vorticity tendency, and we denote the sum of the terms other than RES on the right-hand side as RHS.

Additionally, we calculate the flux form of the vorticity equation to compare the budget analysis with Eq. (1):

$$\frac{\partial \zeta}{\partial t} = -\nabla_h \cdot \mathbf{Z} = -\nabla_h \cdot (\mathbf{V}_h \zeta_Z - \zeta_h w + \hat{\mathbf{k}} \times \mathbf{F}). \quad (2)$$

where \mathbf{Z} is the vorticity flux tensor. The term $\mathbf{V}_h \zeta_Z$ is the horizontal advective flux of vertical vorticity (HADV-Flux), $-\zeta_h w$ is the horizontal flux of vertical vorticity caused by the vertical flux of horizontal vorticity (HFlux), and $\hat{\mathbf{k}} \times \mathbf{F}$ is the horizontal flux of vertical vorticity caused by friction, which is ignored here (Haynes and McIntyre 1987).

Overall, the domain-averaged quasi-Lagrangian vorticity budget at 850 hPa shown in Fig. 8a is balanced well from the formation stage to the occlusion stage. The vorticity budget uses the average of estimations from an ensemble of seven perturbed domains through decreasing or enlarging each side of the box ($324 \text{ km} \times 216 \text{ km}$) denoted in Fig. 5 by $-27, -18, -9, 0, 9, 18$, and 27 km . Figure 8c shows the budget results for the flux form of the vorticity equation, where the divergence of HADVFlux combined the effect of HADV and STRE in Eq. (1). In addition, divergence of HFlux is associated with TILT and VADV. Davis and Galarneau (2009) analyzed two MCV cases based on the Eulerian, flux-form vorticity by integrating the form in Eq. (2) over a closed region; the virtue of that is to examine the net mesoscale circulation within a region in which complex convection and vorticity dynamics are taking place without having to explicitly analyze the full complexity. Since the vorticity diagnosis in this study is quasi-Lagrangian by tracking the evolution of the MCV, it can be seen clearly that the divergence of the HADVflux dominates the evolution of the vorticity, which is consistent with the positive stretching effect in Davis and Galarneau (2009), while the horizontal vorticity contribution (tilting effect) is less important. Additionally, Fig. 9 shows vertical cross sections of the quasi-Lagrangian vorticity budget along the west–east line in Fig. 5. It is apparent that the largest stretching occurs at the level where the MCV attains its greatest intensity (850 hPa). We also performed similar budget calculations for experiments with other model configurations [including one with the use of the WSM6 microphysics (vs WSM5 in the control, not shown) and another with the addition of a large 3-km two-way-nested convection-permitting domain (TOPO_NEST)]. These additional calculations are

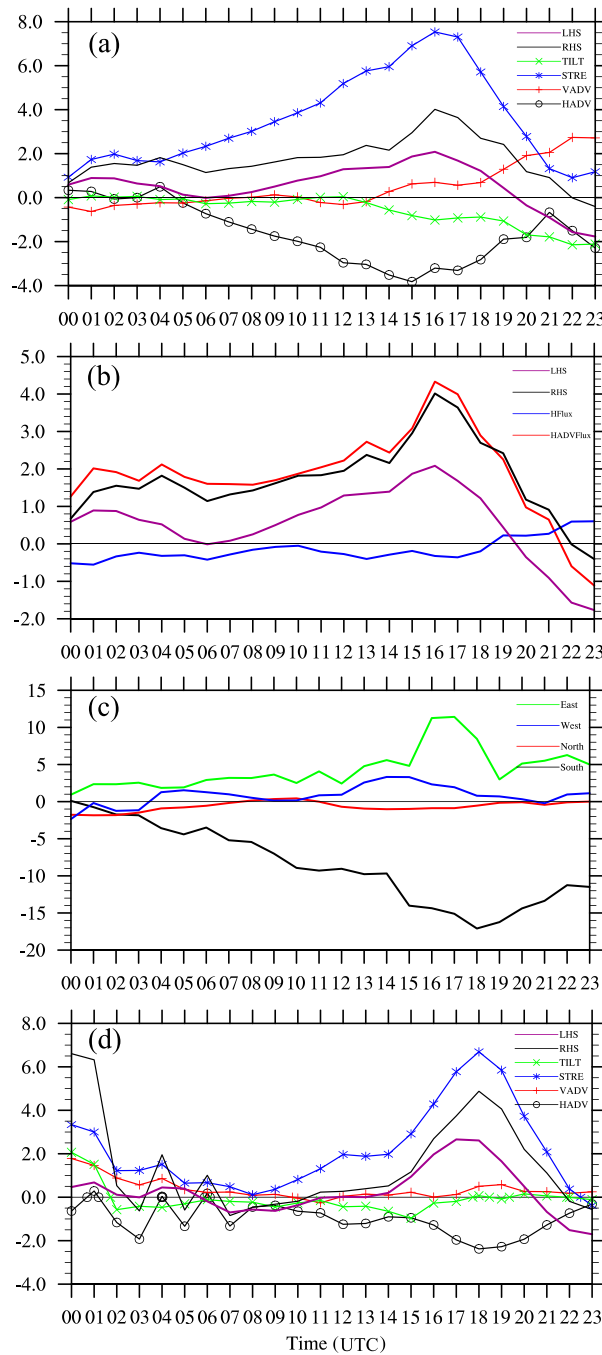


FIG. 8. (a) Quasi-Lagrangian vorticity budget of Eq. (1) averaged over the box area denoted in Fig. 5. LHS is the vorticity tendency on the left-hand side of Eq. (1), RHS is the sum of the terms on the right-hand side, TILT stands for the tilting, STRE is short for stretching, VADV is the vertical advection of vorticity, and HADV is the horizontal advection of vorticity. (b) Flux form of the quasi-Lagrangian vorticity budget. HADVFlux symbolizes the divergence of the horizontal advective flux of vertical vorticity. HFlux is the divergence of the horizontal flux of vertical vorticity resulting from the vertical flux of horizontal vorticity. (c) The horizontal advection through the south, north, west, and east sides of the boxes in Fig. 5. (d) As in (a), but for the TOPO_NEST. The units for the y axes are 10^{-9} s^{-2} .

qualitatively similar to the results shown herein. Compared with TOPO_CNTL, though the vortex of the TOPO_NEST is intensified later in the day, the vorticity tendencies in the intensification period are still very similar (Fig. 8d). These results further improve the rationality of the diagnosis and analysis based on the simulation of TOPO_CNTL.

The specific processes and the three-dimensional structure of the MCV and its corresponding convection during each stage of evolution will be analyzed in the following subsections.

b. Formation stage of couplet C1/V1 [0800–1300 BST (0000–0500 UTC)]

Between morning and early afternoon [0800–1300 BST (0000–0500 UTC); Figs. 5a–c], the immediate lee-side wind shear forms a closed circulation with localized vorticity enhanced as described above. The vorticity maximum is nearly coincident with the strong convection center (Figs. 5a–c and 7b). The west–east vertical cross section of the formation stage of C1/V1, derived along the brown line shown in Fig. 5, reveals that the vortex is strongest below 3 km (700 hPa) but the positive vorticity extends upward to about 8 km (Fig. 10a). The decrease in equivalent potential temperature with height below 5 km implies a large potential instability east of the MCV center. When released as rising air over the shallow frontal boundary to the east of the MCV, the result is organized deep convection with a strong mesoscale upward mass-flux signature.

Following sunrise [1000 BST (0200 UTC)], the vorticity and vertical velocity of the C1/V1 couplet is enhanced (Figs. 5b and 5c) with stronger vorticity and vertical velocity. With the increasing intensity of the C1/V1 couplet, the southwest–northeast orientation of the MCV evolves into a nearly circular distribution, and the maximum vorticity becomes larger than $2.5 \times 10^{-4} \text{ s}^{-1}$ (Fig. 5c). The vorticity at lower levels (below 3 km) increases to greater than $3 \times 10^{-4} \text{ s}^{-1}$ in the early afternoon [1300 BST (0500 UTC); Fig. 10f]. The vorticity budget (Fig. 8a) shows that the stretching term contributes to the main positive vorticity tendency from 0800–1400 BST (0000–0600 UTC). Meanwhile, because of the increasing solar heating after sunrise [1000–1200 BST (0200–0400 UTC); Fig. 10c], the large regional-scale MPS circulation between the Tibetan Plateau and its low-lying regions (Bao et al. 2011; SZ12; Zhang et al. 2014) forces the downward motion over the west side of the MCV center in the mid- to high levels (from 4–5 to 9–10 km). Additionally, the negative vertical velocity of the downward branch of the MPS is consistent with low equivalent potential temperature, forming the large horizontal pseudoequivalent potential gradient between the lee side and the convection area. During this stage,

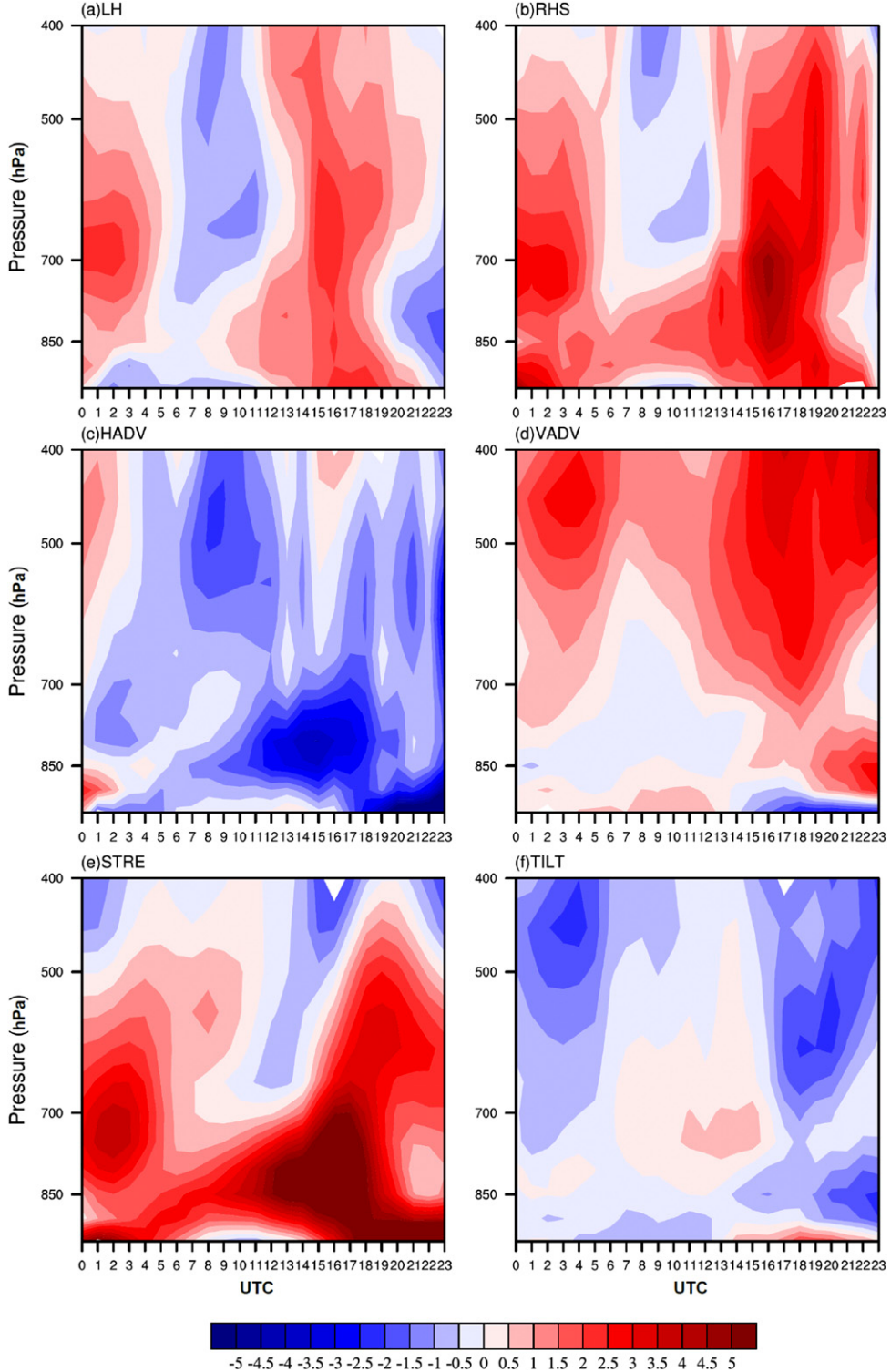


FIG. 9. Height–time diagrams of the vorticity budget terms as described in Fig. 7 averaged over the box in Fig. 5 (10^{-9} s^{-2}).

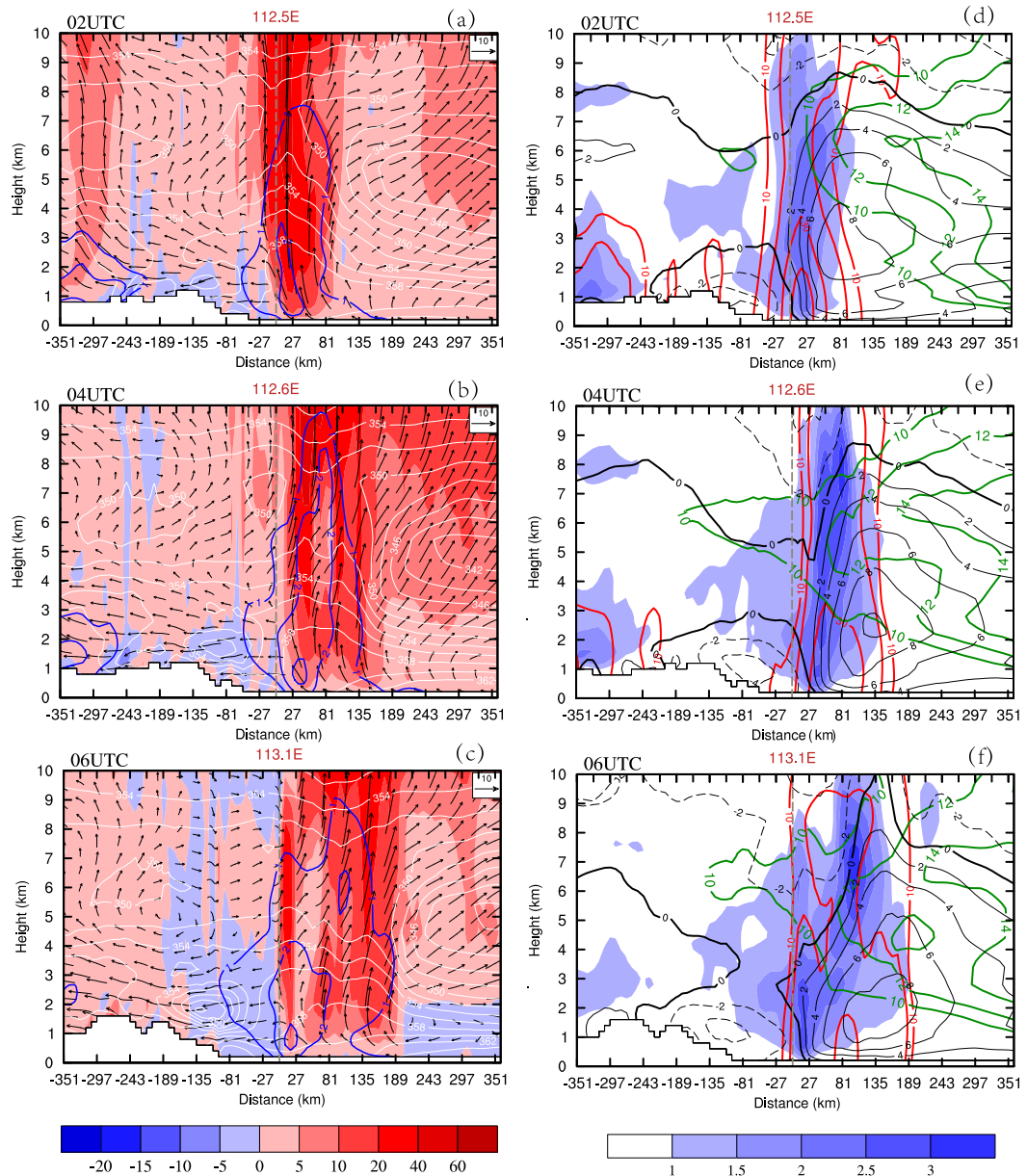


FIG. 10. Vertical cross section of C1/V1 at the formation stage. (a)–(c) Wind field (vectors; zonal wind and vertical wind $\times 100$), vertical velocity (shading; cm s^{-1}), pseudoequivalent potential temperature (white lines; K), and vertical vorticity (greater than 10^{-4} s^{-1} ; blue lines) from west to east. The brown number above each panel is the longitude of the MCV center. (d)–(f) The corresponding PV (shading; PVU), zonal wind speed ($>10 \text{ m s}^{-1}$; green line), meridional wind speed (black lines; m s^{-1}), and reflectivity (dBZ; red line).

the average horizontal scale of the MCV is roughly 300 km, and its intensity and convection are increasing with time (Figs. 5a–c and 7a).

c. Decoupling stage of couplet C1/V1 [1400–2000 BST (0600–1200 UTC)]

In the local afternoon (Figs. 5d–g and 7b), the convection begins to decrease and shift to the east-southeast side of the MCV, with the maximum column reflectivity

larger than 30 dBZ. With the weakening of the convection, the structure of the MCV becomes more elongated in the southwest–northeast direction. Because of the more intense diabatic heating over the elevated terrain in the afternoon [1500 BST (0700 UTC); Fig. 11b], the downward branch of the MPS intensifies over the western side of the MCV and suppresses convection near the MCV center. Weak upward motion appears to the eastern side of the MCV center (~ 80 km east of the

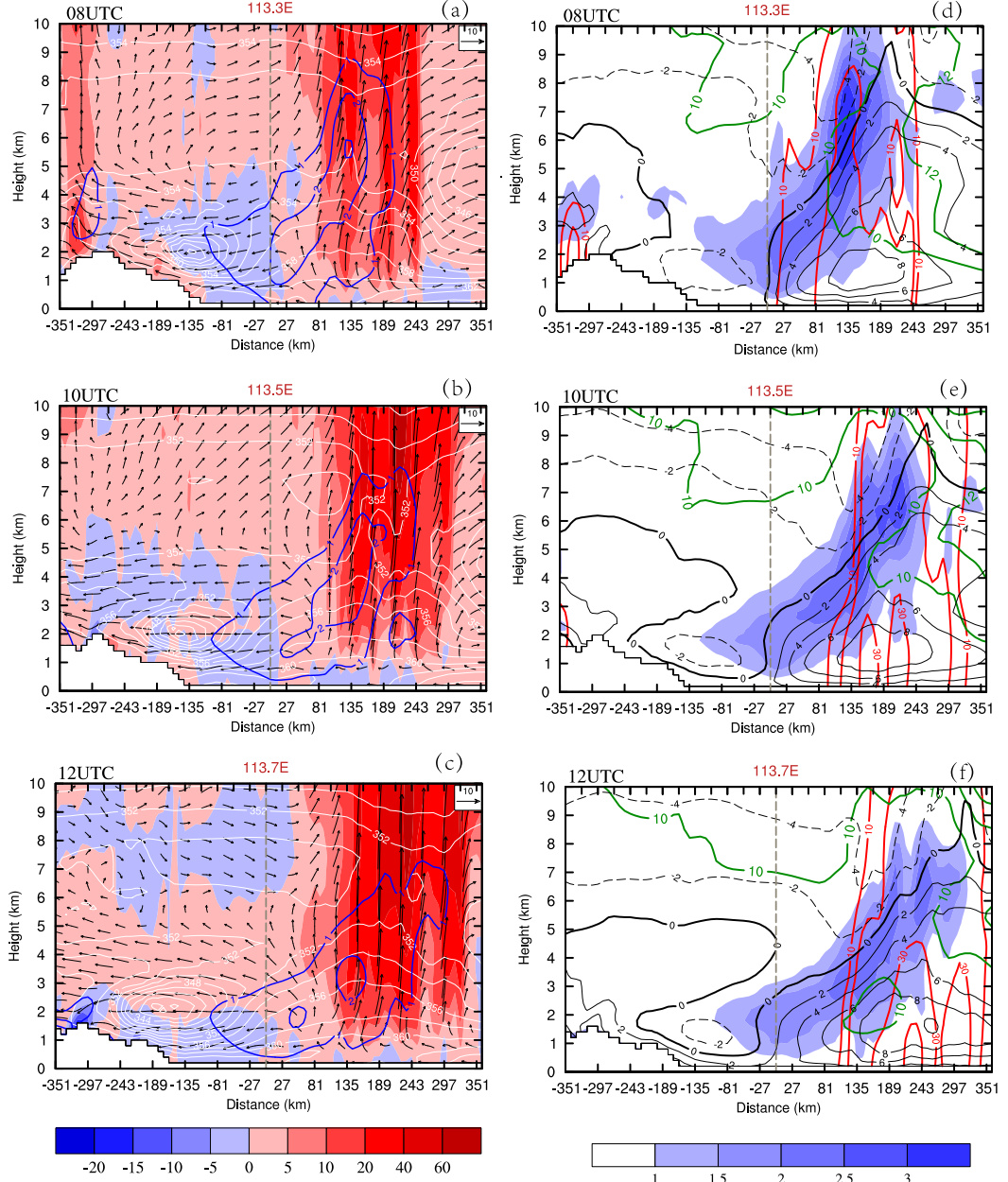


FIG. 11. As in Fig. 10, but for the vertical cross sections during the decoupling stage of C1/V1.

MCV center; Figs. 5e,f and 11a,d). Convection in the mid- to upper levels (above 5 km) is coincident with vorticity and PV maxima associated with the mid- to upper-level (500–400 hPa) trough but is displaced 100 km or more to the east of the lower-tropospheric MCV center. The tilted structure of the MCV is consistent with the vertical shear of the zonal wind (Fig. 11e). As convection weakens during the afternoon, there is less resistance to this vertical shear and the tilt increases [1600–2000 BST (0800–1200 UTC); Figs. 11d–f].

The quasi-Lagrangian vorticity budget (Fig. 8a) during stage 2 shows that the stretching effect is still the main positive contribution to the increase in vorticity. However, the enhancement of the negative effect of horizontal advection of vorticity balances the larger positive effect from stretching, and the result is only a slight increase in vorticity. Figure 8c shows the averaged boundary horizontal advection of vorticity over the domain during the whole evolution of the MCV. It can be seen clearly that the horizontal advection of vorticity

through the western and northern boundaries is weaker compared with that through the eastern and southern boundaries. There is positive horizontal advection through the eastern boundary, but negative vorticity transportation through the southern boundary increases after the formation of the MCV. After 1400 BST (0600 UTC), the main negative vorticity advection is through the south boundary because of the enhanced southwestern flow and the negative vorticity gradient south of the MCV (Figs. 5d–f).

d. Formation stage of couplet C2/V2 [2100–0200 BST (1300–1800 UTC)]

From the time–radius diagram of PV at 850 hPa (Fig. 7a), it can be seen clearly that there is a second increase in the vorticity magnitude and horizontal scale of the vortex (300–400 km). Because of the convection–MCV decoupling during stage 2, the MCV covers a wider area east of the second-step terrain, with the convection on its east-southeast side [2000–0000 BST (1200–1600 UTC); Figs. 5h and 5i]. In the evening [2100 BST (1300 UTC), not shown], the strengthened convection is associated with enhanced convergence over the northeastern side of the MCV. The enhanced nocturnal LLJ favors the new convection (C2) near the lower-tropospheric MCV center (Fig. 12). Additionally, because of the loss of solar heating from evening to early the next morning, the upward branch of the nocturnal MPS circulation shifts over the eastern plains, which is consistent with the broadening upward vertical motion over the whole MCV region (Figs. 12c and 12f). The broadscale evolution is consistent with the gravity wave analysis of Tripoli and Cotton (1989), and the extent of the MPS to the coastal plain was confirmed by SZ12. The strong influence of the diurnal cycle of surface heating on the relative location and variability of convection to the MCV caused by the radiation-induced instability gradients was explored by Trier et al. (2000). In addition, the loss of shortwave radiative heating after sunset was shown by Melhauser and Zhang (2014) to reduce convective inhibition just above a tropical maritime boundary layer, and thus to enable more widespread deep convection. We suspect this destabilization is occurring here as well, though a future study is needed to further examine the convective–radiative feedback during the MCV evolution.

The vertical cross sections of vertical velocity and vorticity show that the new vorticity maximum forms below 3 km at 1500 UTC east of the MCV center. The corresponding convection (C2) intensifies near the vorticity center in the southeast quadrant of the new MCV (V2). This defines stage 3.

The vorticity budget analysis shows that the vorticity increases dramatically because of the strong positive

stretching effect (Fig. 8a). From the vertical cross section of the vorticity budget (Fig. 9), it is clear that the positive vorticity tendency changes sharply after 2100 BST (1300 UTC) below 3 km, and that the stretching effect contributes most to the enhancement. It is possible that the nocturnal LLJ south of the vortex contributes to strong convergence broadly below 700 hPa.

In contrast to the previous stages, the diabatic heating in stage 3 is deeper over the low-level circulation center (Fig. 13a). There is an abrupt increase in diabatic heating between 2200 and 2300 BST (1400–1500 UTC) that precedes the PV increase by about 2 h. Xu et al. (2017) also found that the descent of the MCV occurs in response to the lowering of the maximum diabatic heating within the convective system. The change in diabatic heating is associated with the changes in cloud water mixing ratio (Fig. 13b, QCLOUD and QRAIN output from the model). The large gradient of condensate is indicative of the rapid increase in low-level vertical velocity in this stage. Latent heating experiments designed by Morales et al. (2015) showed that high rates of cloud water condensation led to a strong vertical gradient in latent heating, which resulted in a near-surface positive PV anomaly. We speculate that the strong low-level jet transports additional water vapor into the vicinity of the lower-tropospheric MCV center. Abrupt lifting ensues as the jet reaches the vorticity (PV) maximum and the frontal zone in a manner consistent with that discussed by Fritsch et al. (1994) and Schumacher and Johnson (2008). The stretching effect below 700 hPa reaches its peak after 2000 BST (1200 UTC, the beginning of this stage), implying that the nocturnal LLJ favors the stronger convergence that promotes the MCV (V2) development. Additionally, the new enhanced MCV favors the further development of convection (C2) (Figs. 12b,c and 12e,f). The intensified vortex within the convective region quickly grows to dominate the horizontal circulation by the end of stage 3 [0000–0200 BST (1600–1800 UTC); Fig. 5].

e. Occlusion stage of couplet C2/V2 [1900–2300 UTC (0300–0700 BST)]

Before significant solar heating begins, the new couplet C2/V2 arrives over the YHRV [0300–0400 BST (1900–2000 UTC); Fig. 5]. The MCV finally increases in size to subsynoptic scale (~ 700 km) in the eastern part of the mei-yu front. The vorticity budget at 850 hPa shows that the main contribution to the vorticity tendency from the divergence of HADFlux (stretching and horizontal advection) in the former stages shifts to the divergence of vertical flux of horizontal vorticity (vertical advection and tilting terms). The vortex becomes more circular and clearly distorts the orientation of the mei-yu

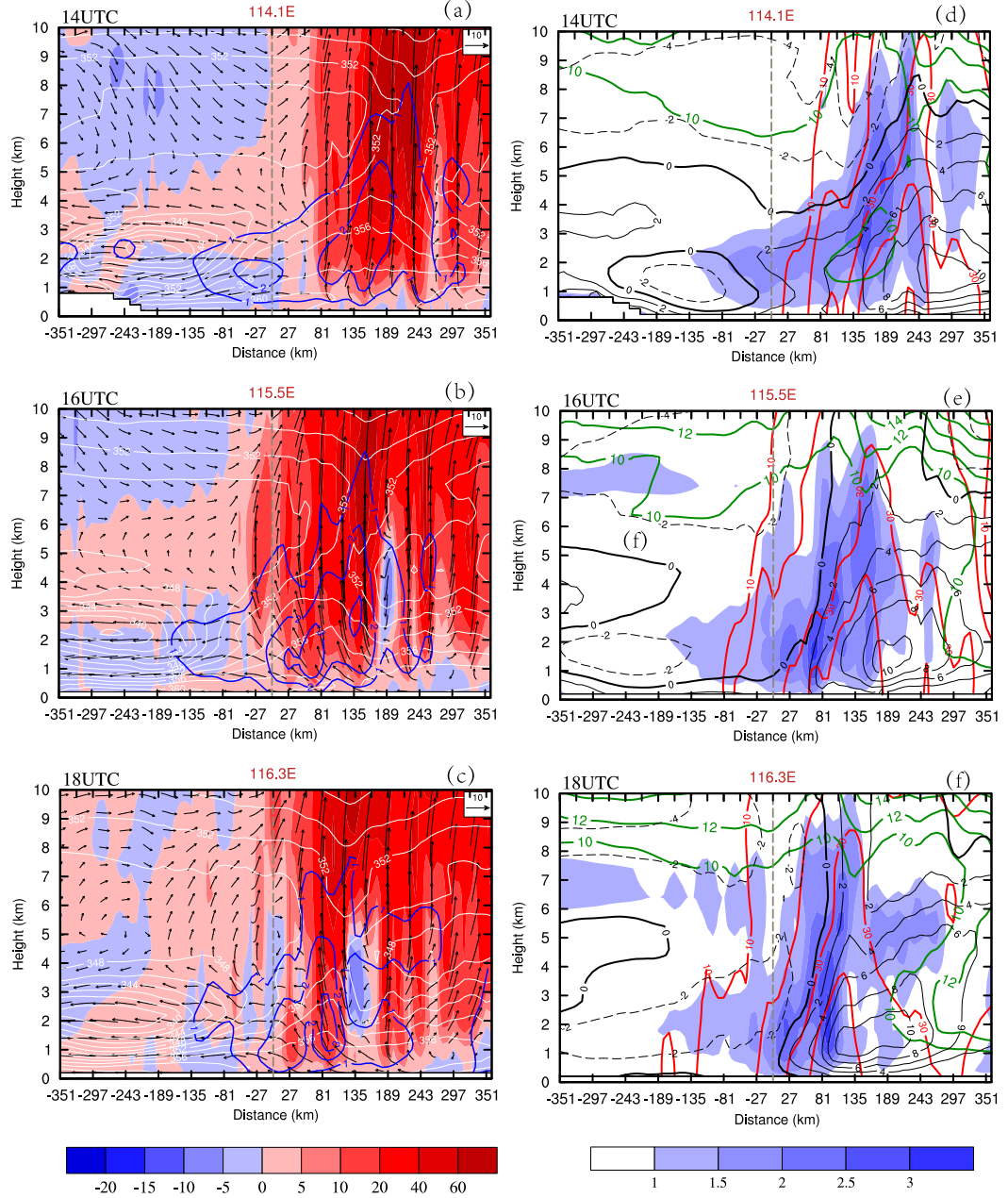


FIG. 12. As in Fig. 10, but for the vertical cross sections during the formation stage of C2/V2.

front into a structure resembling a midlatitude occlusion (Figs. 5l and 14).

In the daytime [0800–1400 BST (0000–0600 UTC); Figs. 4a–c], after solar heating begins, the convection weakens and the MCV/cyclone and convection move eastward and gradually (and finally) decay over the ocean. We do not investigate this phase of evolution in detail, partly because the disturbance begins to encounter the eastern boundary of the domain, which can be artificially damped by the relaxation of the boundary

conditions. In real observations, some of the MCVs and subsynoptic cyclones can be further developed into even larger- or synoptic-scale cyclones with the reduced surface friction and enhanced moisture flux over the ocean.

5. Concluding remarks

We conducted diurnal-cycle boundary-forcing experiments via 30-day integration of the Advanced Research version of the WRF Model to explore the evolution and

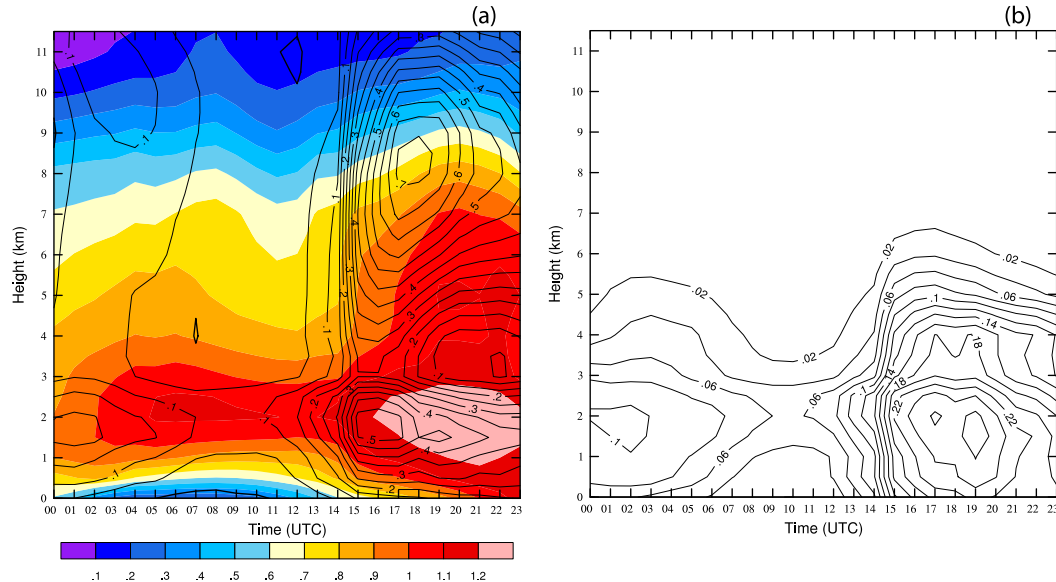


FIG. 13. Height–time diagrams of (a) diabatic heating (contours; 10^{-3} K s⁻¹) and PV (shading; PVU), and (b) the total liquid water content (QCLOUD + QRRAIN; g kg⁻¹) averaged over the box in Fig. 5.

structure of an MCV and its corresponding convection along a typical mei-yu front. Sensitivity experiments showed the intensity of the MCV and convection to be less influenced by horizontal terrain on scales smaller

than 500 km. Although all three experiments could reproduce the maintenance of the southwest vortex and the mei-yu front, the TOPO_CNTL experiment (with somewhat simplified terrain) could describe the diurnal

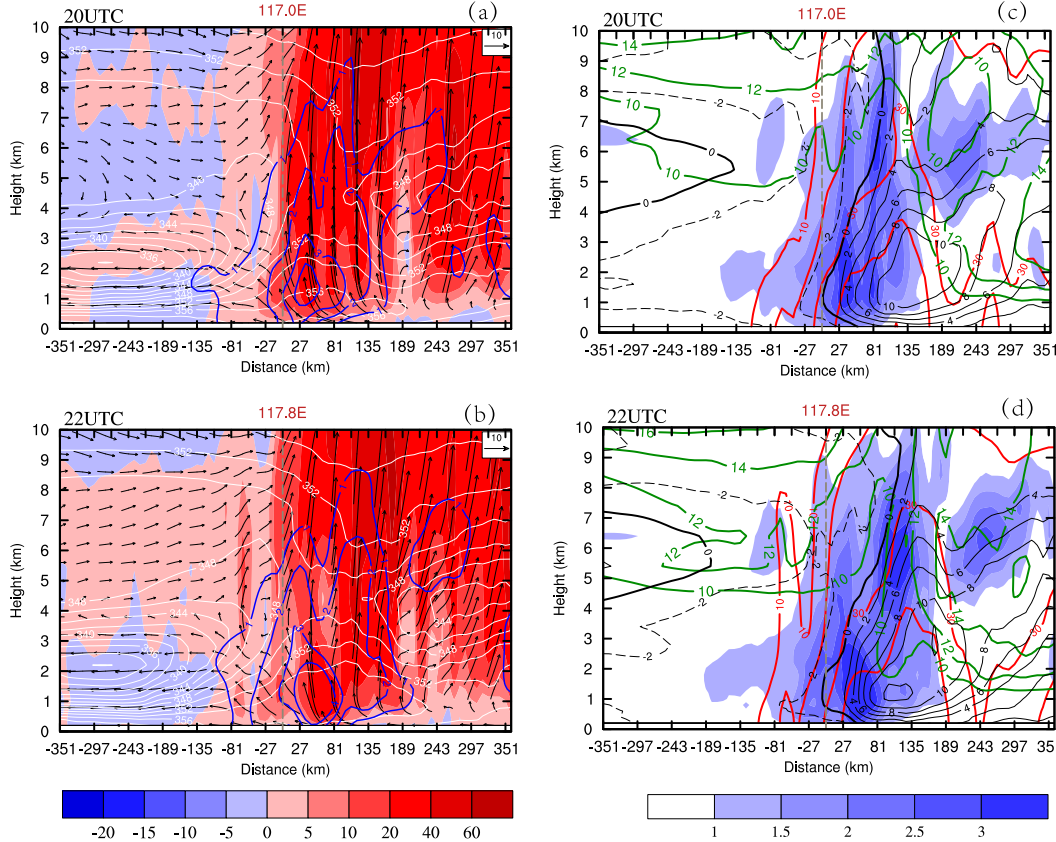


FIG. 14. As in Fig. 10, but for the vertical cross sections of couplet C2/V2 during the occlusion stage.

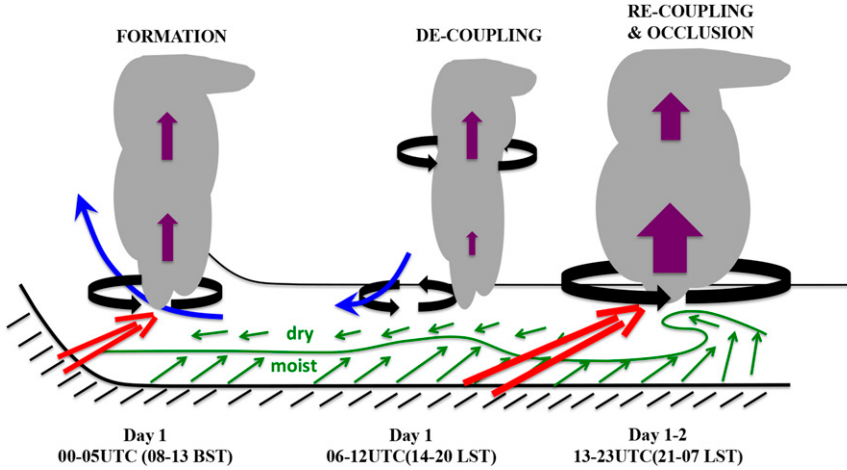


FIG. 15. Schematic of convection and MCV eastward progression and diurnal evolution. (left) The formation stage in the early morning of day 1 (stage 1) is shown. (middle) This is followed by the afternoon decoupling stage as deep convection is displaced from the vortex center and the vortex tilts eastward with height (stage 2). (right) Convection re-intensifies near the vortex center during the following evening, the low-level jet intensifies, and the vortex strengthens, ultimately reaching an occluded configuration (stages 3 and 4). Features include low-level jet (red arrows), mountain–plains solenoid (blue arrows), mesoscale updraft (purple arrows), vortex horizontal circulation (black arrows), ground (black line), convective region (gray shading), mei-yu boundary (green line), and surface winds (green arrows).

cycle of the eastward propagation of precipitation, the evolution, and the structure of the MCV and the convection. The main evolution of the MCV and its convection could be divided into four stages. These stages are depicted from left to right in the schematic shown in Fig. 15, wherein stages 3 and 4 are combined in the rightmost image.

The first stage was the formation of the MCV (V1) and its convection (C1) appearing in the morning to early afternoon. The eastward-extending vorticity and convection from the Sichuan basin in the early evening triggered an immediate enhanced leeside localized vortex below 700 hPa east of the second-step terrain, and the convection was almost consistent with the vorticity maximum. The stretching effect (low-level convergence) was the main contribution to the vorticity enhancement.

The second stage was the decoupling of C1/V1 from the local afternoon to early evening. The convection decreased overall and shifted to the east-southeast side of the vorticity maximum, and the vortex covered a broader area. Meanwhile, because of the subsiding branch of the daytime MPS over the lower-tropospheric MCV center, the upward motion was displaced to the east of the MCV center. Furthermore, vertical wind shear owing to the westerlies in the middle and upper troposphere contributed to tilting the vortex in the downshear direction. The result was a weakened vorticity structure overall, with deep convection enhancing vorticity and PV in the middle and upper troposphere.

During the following evening to early morning (stage 3), the updraft branch of the nocturnal MPS circulation and the enhanced nocturnal LLJ favored new convection (C2) on the southeast side of the MCV, closer to the original center, and the diabatic heating from water vapor condensation at low levels developed a strong PV maximum in the lower troposphere. The weakened negative horizontal advection and strengthened stretching effect from low-level convergence favored the fast vortex development (V2).

Finally, the occlusion stage of C2/V2 appeared early the next morning before significant solar heating. The new MCV evolved into a subsynoptic cyclone with signs of occlusion (i.e., potent convection within all sectors of the vorticity maximum), as well as stretching the convergence line to the southwest side, where there were separate vorticity and convection maxima.

The present study was focused on the evolution and structure of the long-lived MCV and its convection. Many individual aspects of the diurnal evolution of the MCV and deep convection noted herein have been noted in previous studies. However, the present cyclic simulation methodology suppresses synoptic-scale variations that often complicate the interpretation of observed cases, and it accentuates the interconnections between processes in different phases of the diurnal cycle. In future work, consideration should be given to the factors that trigger the leeside vortex, as well as to the features of the diurnal cycle that are related to vortex initiation.

Acknowledgments. Part of the research was conducted during the lead author YZ's sabbatical visit at the Pennsylvania State University. YZ and JS acknowledge the grant support from the National Natural Science Foundation of China (Grants 41505038, 41375053, and 91637211). FZ is partially supported by the National Science Foundation under Grants AGS-1114849 and AGS-1305798. Computing was provided by the Texas Advanced Computing Center, and the China Lvliang Cloud Computing Center is also acknowledged. All modeling data can be accessed at both computing centers.

REFERENCES

- Bao, X., F. Zhang, and J. Sun, 2011: Diurnal variations of warm-season precipitation east of the Tibetan Plateau over China. *Mon. Wea. Rev.*, **139**, 2790–2810, <https://doi.org/10.1175/MWR-D-11-00006.1>.
- Bartels, D. L., and R. A. Maddox, 1991: Midlevel cyclonic vortices generated by mesoscale convective systems. *Mon. Wea. Rev.*, **119**, 104–118, [https://doi.org/10.1175/1520-0493\(1991\)119<0104:MCVGBM>2.0.CO;2](https://doi.org/10.1175/1520-0493(1991)119<0104:MCVGBM>2.0.CO;2).
- Bosart, L. F., and F. Sanders, 1981: The Johnstown flood of July 1977: A long-lived convective system. *J. Atmos. Sci.*, **38**, 1616–1642, [https://doi.org/10.1175/1520-0469\(1981\)038<1616:TJFOJA>2.0.CO;2](https://doi.org/10.1175/1520-0469(1981)038<1616:TJFOJA>2.0.CO;2).
- Brandes, E. A., 1990: Evolution and structure of the 6–7 May 1985 mesoscale convective system and associated vortex. *Mon. Wea. Rev.*, **118**, 109–127, [https://doi.org/10.1175/1520-0493\(1990\)118<0109:EASOTM>2.0.CO;2](https://doi.org/10.1175/1520-0493(1990)118<0109:EASOTM>2.0.CO;2).
- Brown, J. M., 1979: Mesoscale unsaturated downdrafts driven by rainfall evaporation: A numerical study. *J. Atmos. Sci.*, **36**, 313–338, [https://doi.org/10.1175/1520-0469\(1979\)036<0313:MUDDBR>2.0.CO;2](https://doi.org/10.1175/1520-0469(1979)036<0313:MUDDBR>2.0.CO;2).
- Chen, F., and J. Dudhia, 2001: Coupling an advanced land surface-hydrology model with the Penn State–NCAR MM5 modeling system. Part I: Model implementation and sensitivity. *Mon. Wea. Rev.*, **129**, 569–585, [https://doi.org/10.1175/1520-0493\(2001\)129<0569:CAALSH>2.0.CO;2](https://doi.org/10.1175/1520-0493(2001)129<0569:CAALSH>2.0.CO;2).
- Chen, G. T.-J., 1983: Observational aspects of Mei-yu phenomena in subtropical China. *J. Meteor. Soc. Japan*, **61**, 306–312, https://doi.org/10.2151/jmsj1965.61.2_306.
- Chen, M., and Y. G. Zheng, 2004: Vorticity budget investigation of a simulated long-lived mesoscale vortex in South China. *Adv. Atmos. Sci.*, **21**, 928–940, <https://doi.org/10.1007/BF02915595>.
- Chen, S. S., and W. M. Frank, 1993: A numerical study of the genesis of extratropical convective mesovortices. Part I: Evolution and dynamics. *J. Atmos. Sci.*, **50**, 2401–2426, [https://doi.org/10.1175/1520-0469\(1993\)050<2401:ANSOTG>2.0.CO;2](https://doi.org/10.1175/1520-0469(1993)050<2401:ANSOTG>2.0.CO;2).
- Davis, C. A., and M. L. Weisman, 1994: Balanced dynamics of mesoscale vortices produced in simulated convective systems. *J. Atmos. Sci.*, **51**, 2005–2030, [https://doi.org/10.1175/1520-0469\(1994\)051<2005:BDOMVP>2.0.CO;2](https://doi.org/10.1175/1520-0469(1994)051<2005:BDOMVP>2.0.CO;2).
- , and S. B. Trier, 2002: Cloud-resolving simulations of mesoscale vortex intensification and its effect on a serial mesoscale convective system. *Mon. Wea. Rev.*, **130**, 2839–2858, [https://doi.org/10.1175/1520-0493\(2002\)130<2839:CRSOMV>2.0.CO;2](https://doi.org/10.1175/1520-0493(2002)130<2839:CRSOMV>2.0.CO;2).
- , and —, 2007: Mesoscale convective vortices observed during BAMEX. Part I: Kinematic and thermodynamic structure. *Mon. Wea. Rev.*, **135**, 2029–2049, <https://doi.org/10.1175/MWR3398.1>.
- , and T. J. Galarneau, 2009: The vertical structure of mesoscale convective vortices. *J. Atmos. Sci.*, **66**, 686–704, <https://doi.org/10.1175/2008JAS2819.1>.
- Ding, Y. H., 1993: *Study on the Lasting Heavy Rainfalls over the Yangtze-Huaihe River Basin in 1991* (in Chinese). Chinese Meteorological Press, 255 pp.
- Dudhia, J., 1989: Numerical study of convection observed during the winter monsoon experiment using a mesoscale two-dimensional model. *J. Atmos. Sci.*, **46**, 3077–3107, [https://doi.org/10.1175/1520-0469\(1989\)046<3077:NSOCOD>2.0.CO;2](https://doi.org/10.1175/1520-0469(1989)046<3077:NSOCOD>2.0.CO;2).
- Fritsch, J. M., J. D. Murphy, and J. S. Kain, 1994: Warm core vortex amplification over land. *J. Atmos. Sci.*, **51**, 1780–1807, [https://doi.org/10.1175/1520-0469\(1994\)051<1780:WCVAOL>2.0.CO;2](https://doi.org/10.1175/1520-0469(1994)051<1780:WCVAOL>2.0.CO;2).
- Geng, B., and H. Yamada, 2007: Diurnal variations of the Meiyu/Baiu rain belt. *SOLA*, **3**, 61–64, <https://doi.org/10.2151/sola.2007-016>.
- Grell, G. A., and D. Dévényi, 2002: A generalized approach to parameterizing convection combining ensemble and data assimilation techniques. *Geophys. Res. Lett.*, **29**, <https://doi.org/10.1029/2002GL015311>.
- Haynes, P. H., and M. E. McIntyre, 1987: On the evolution of vorticity and potential vorticity in the presence of diabatic heating and frictional or other forces. *J. Atmos. Sci.*, **44**, 828–841, [https://doi.org/10.1175/1520-0469\(1987\)044<0828:OTEVOA>2.0.CO;2](https://doi.org/10.1175/1520-0469(1987)044<0828:OTEVOA>2.0.CO;2).
- Hong, S.-Y., and J.-O. J. Lim, 2006: The WRF Single-Moment 6-Class Microphysics Scheme (WSM6). *J. Korean Meteor. Soc.*, **42**, 129–151.
- , J. Dudhia, and S.-H. Chen, 2004: A revised approach to ice microphysical processes for the bulk parameterization of clouds and precipitation. *Mon. Wea. Rev.*, **132**, 103–120, [https://doi.org/10.1175/1520-0493\(2004\)132<0103:ARATIM>2.0.CO;2](https://doi.org/10.1175/1520-0493(2004)132<0103:ARATIM>2.0.CO;2).
- Jorgensen, D., and B. F. Smull, 1993: Mesovortex circulations seen by airborne Doppler radar within a bow echo mesoscale convective system. *Bull. Amer. Meteor. Soc.*, **74**, 2146–2157, [https://doi.org/10.1175/1520-0477\(1993\)074<2146:MCSBAD>2.0.CO;2](https://doi.org/10.1175/1520-0477(1993)074<2146:MCSBAD>2.0.CO;2).
- Kirk, J. R., 2007: A phase-plot method for diagnosing vorticity concentration mechanisms in mesoscale convective vortices. *Mon. Wea. Rev.*, **135**, 801–820, <https://doi.org/10.1175/MWR3322.1>.
- Melhauser, C., and F. Zhang, 2014: Diurnal radiation cycle impact on the pregenesis environment of Hurricane Karl (2010). *J. Atmos. Sci.*, **71**, 1241–1259, <https://doi.org/10.1175/JAS-D-13-0116.1>.
- Morales, A., R. S. Schumacher, and S. M. Kreidenweis, 2015: Mesoscale vortex development during extreme precipitation: Colorado, September 2013. *Mon. Wea. Rev.*, **143**, 4943–4962, <https://doi.org/10.1175/MWR-D-15-0086.1>.
- Ninomiya, K., 2000: Large- and meso- α -scale characteristics of Meiyu/Baiu front associated with intense rainfalls in 1–10 July 1991. *J. Meteor. Soc. Japan*, **78**, 141–157, https://doi.org/10.2151/jmsj1965.78.2_141.
- Noh, Y., W. G. Cheon, and S. Raasch, 2001: The improvement of the K-profile model for the PBL using LES. *Preprints, Int. Workshop of Next Generation NWP Models*, Seoul, South Korea, Laboratory for Atmospheric Modeling Research, 65–66.

- Raymond, D. J., and H. Jiang, 1990: A theory for long-lived convective systems. *J. Atmos. Sci.*, **47**, 3067–3077, [https://doi.org/10.1175/1520-0469\(1990\)047<3067:ATFLLM>2.0.CO;2](https://doi.org/10.1175/1520-0469(1990)047<3067:ATFLLM>2.0.CO;2).
- Rogers, R. F., and J. M. Fritsch, 2001: Surface cyclogenesis from convectively driven amplification of midlevel mesoscale convective vortices. *Mon. Wea. Rev.*, **129**, 605–637, [https://doi.org/10.1175/1520-0493\(2001\)129<0605:SCFCDA>2.0.CO;2](https://doi.org/10.1175/1520-0493(2001)129<0605:SCFCDA>2.0.CO;2).
- Schumacher, R. S., and R. H. Johnson, 2008: Mesoscale processes contributing to extreme rainfall in a midlatitude warm-season flash flood. *Mon. Wea. Rev.*, **136**, 3964–3986, <https://doi.org/10.1175/2008MWR2471.1>.
- Skamarock, W. C., M. L. Weisman, and J. B. Klemp, 1994: Three-dimensional evolution of simulated long-lived squall lines. *J. Atmos. Sci.*, **51**, 2563–2584, [https://doi.org/10.1175/1520-0469\(1994\)051<2563:TDEOSL>2.0.CO;2](https://doi.org/10.1175/1520-0469(1994)051<2563:TDEOSL>2.0.CO;2).
- , —, J. B. Klemp, J. Dudhia, D. O. Gill, D. M. Barker, W. Wang, and J. G. Powers, 2005: A description of the Advanced Research WRF version 2. NCAR Tech. Note NCAR/TN-468+STR, 88 pp., <https://doi.org/10.5065/D6DZ069T>.
- Sun, J., and F. Zhang, 2012: Impacts of mountain–plains solenoid on diurnal variations of rainfalls along the mei-yu front over the East China plains. *Mon. Wea. Rev.*, **140**, 379–397, <https://doi.org/10.1175/MWR-D-11-00041.1>.
- , —, S. X. Zhao, G. K. Xu, and Q. T. Meng, 2010: Study on a mesoscale convective vortex causing heavy rainfall during the Mei-yu season in 2003. *Adv. Atmos. Sci.*, **27**, 1193–1209, <https://doi.org/10.1007/s00376-009-9156-6>.
- Thorpe, A. J., 1985: Diagnosis of balanced vortex structure using potential vorticity. *J. Atmos. Sci.*, **42**, 397–406, [https://doi.org/10.1175/1520-0469\(1985\)042<0397:DOBVVSU>2.0.CO;2](https://doi.org/10.1175/1520-0469(1985)042<0397:DOBVVSU>2.0.CO;2).
- Trier, S. B., C. A. Davis, and J. D. Tuttle, 2000: Long-lived mesoconvective vortices and their environment. Part I: Observations from the central United States during the 1998 warm season. *Mon. Wea. Rev.*, **128**, 3376–3395, [https://doi.org/10.1175/1520-0493\(2000\)128<3376:LLMVAT>2.0.CO;2](https://doi.org/10.1175/1520-0493(2000)128<3376:LLMVAT>2.0.CO;2).
- , —, D. A. Ahijevych, M. L. Weisman, and G. H. Bryan, 2006: Mechanisms supporting long-lived episodes of propagating nocturnal convection within a 7-day WRF model simulation. *J. Atmos. Sci.*, **63**, 2437–2461, <https://doi.org/10.1175/JAS3768.1>.
- Tripoli, G. J., and W. R. Cotton, 1989: Numerical study of an observed orogenic mesoscale convective system. Part 2: Analysis of governing dynamics. *Mon. Wea. Rev.*, **117**, 305–328, [https://doi.org/10.1175/1520-0493\(1989\)117<0305:NSOAOO>2.0.CO;2](https://doi.org/10.1175/1520-0493(1989)117<0305:NSOAOO>2.0.CO;2).
- Xu, X., M. Xue, Y. Wang, and H. Huang, 2017: Mechanisms of secondary convection within a Mei-Yu frontal mesoscale convective system in eastern China. *J. Geophys. Res. Atmos.*, **122**, 47–64, <https://doi.org/10.1002/2016JD026017>.
- Yu, C. K., B. J.-D. Jou, and B. F. Smull, 1999: Formative stage of a long-lived mesoscale vortex observed by airborne Doppler radar. *Mon. Wea. Rev.*, **127**, 838–857, [https://doi.org/10.1175/1520-0493\(1999\)127<0838:FSOALL>2.0.CO;2](https://doi.org/10.1175/1520-0493(1999)127<0838:FSOALL>2.0.CO;2).
- Zhang, D.-L., 1992: The formation of a cooling-induced mesovortex in the trailing stratiform region of a midlatitude squall line. *Mon. Wea. Rev.*, **120**, 2763–2785, [https://doi.org/10.1175/1520-0493\(1992\)120<2763:TFOACI>2.0.CO;2](https://doi.org/10.1175/1520-0493(1992)120<2763:TFOACI>2.0.CO;2).
- Zhang, X. L., S. Y. Tao, and S. L. Zhang, 2004: Three types of heavy rainstorms associated with Mei-yu front (in Chinese). *Chin. J. Atmos. Sci.*, **28**, 187–205.
- Zhang, Y. C., J. H. Sun, and S. M. Fu, 2014: Impacts of diurnal variation of mountain–plain solenoid circulations on precipitation and vortices east of the Tibetan Plateau during the Mei-yu season. *Adv. Atmos. Sci.*, **31**, 139–153, <https://doi.org/10.1007/s00376-013-2052-0>.
- Zhao, S. X., Z. Y. Tao, J. H. Sun, and N. F. Bei, 2004: *Study on Mechanism of Formation and Development of Heavy Rainfalls on Mei-Yu Front in Yangtze River* (in Chinese). China Meteorological Press, 282 pp.